Chapter 6

Modeling of Subsurface Ice Growth

6.1 Chapter Summary

A numerical model is developed and applied to the problem of ice growth in the cryosphere beneath the ice table interface. The accumulation of subsurface ice as a function of depth, the dynamics and rate of ice growth, and the effects of deposited ice on the surface and subsurface thermal structure are considered. Climate oscillations over the past 5 million years have repeatedly deposited and removed ice in mid- to high-latitude regoliths, but the past 300 kyr have been relatively quiescent and generally favorable to pore ice accumulation in these regions. The model considers the effects of several parameters on ice growth rate including: ice-free porosity, magnitude of constriction arising from a changing pore-space geometry, thickness of an ice-free surface layer, and the presence of a massive ice sheet below some depth. The different constriction parameterizations and ice-free porosities are found to have only moderate effects on the total quantity of ice deposited and the shape of the ice content profile. Deep ice layers significantly perturb the subsurface temperature field and result in increased ice accumulation at all depths if the massive ice sheet is within 10 m of the surface. Near surface ice-free layers have the greatest influence of the effects considered; a change in surface layer thickness from 2 cm to 5 cm can decrease the subsurface ice content accumulated in 300 kyr by nearly 50%. The environmental parameters chosen for the model match the known properties of the Phoenix Scout Mission landing site. The lowland bright terrain to which the spacecraft is targeted is predicted to harbor an ice-rich subsurface layer within 2–6 cm of the surface. Given this range of ice-free surface, the model indicates that the maximum amount of ice accumulated at the ice table in 300 kyr will be between 70–92% of complete filling, decreasing by not more than 15% at 0.5 m depth in the absense of a buried ice sheet. The true accumulated quantity in the upper layers is likely less than predicted, given that ice-loss events of moderate extent are likely to have occured in the last 300 kyr.

6.2 Influences on Cryosphere Ice Evolution

6.2.1 Atmospheric independence

The non-linear dependence of vapor pressure on temperature allows high temperatures to control the shape of the time-averaged vapor density profile in a regolith subjected to a depth-decaying periodic thermal wave. In an ice-bearing porous medium this gives rise to a down-directed mean-annual vapor density gradient. Vapor moving within the pore spaces follows this gradient irrespective of the gradient between the atmosphere and the ice table.

Upon an increase in subsurface temperature or a drop in atmospheric humidity, the ice table at the top of the cryosphere will become unstable and will retreat deeper into the subsurface by providing a flux of vapor to the atmosphere. The upward directed gradient from the ice table is set by the vapor density difference between the ice table and the atmosphere (*Mellon and Jakosky*, 1993; *Mellon et al.*, 2004; *Schorghofer and Aharonson*, 2005). The downward gradient from the ice table, however, depends only on the subsurface temperature profile, since pore vapor surrounded by ice experiences vapor concentrations and concentration gradients dependent only on the vapor pressure (*i.e.,* temperature) of the local ice. Thus, even as the ice table interface retreats, deeper ice, insulated from the desiccating gradient to the atmosphere, will continue to migrate down the mean annual vapor density gradient. This allows the evolution of ice beneath the ice table to be determined using only subsurface temperatures and not atmospheric water content. It is important, however, to include the thermal effects of ice-free layers near the surface, which attenuate the temperature wave before it reaches the depth of ice stability.

Within the pore spaces themselves, the vapor pressure of water in the pore gas will be in equilibrium with the surrounding ice. In a pore space of order 1 mm, a free-gas diffusion coefficient of $\sim$30 cm^2 s^{-1} (*Wallace and Sagan*, 1979) will permit equilibration between pore ice and the gas within the pore on a timescale of $<$ 1 second, much faster than diurnal temperature and vapor pressure changes. In most diffusion-dominated pore spaces, the pore radius will tend to be smaller than 1 mm. Bulk flow of less humid gas over the ice may also strip the boundary layer away and increase the time to equilibration. Yet the speed of the "wind" within the regolith due to thermal expansion and contraction of air masses rarely exceeds 1 cm per sol, much slower than the rate of diffusive flux (see Section 2.6.1). Thus, the partial pressure of water in pore spaces will remain saturated with respect to the local ice as long as the temperature fluctuations are not overly rapid (*i.e.,* shorter than diurnal variations).

6.2.2 Icy soil thermal conductivity

The thermal conductivity of the bulk regolith material depends on the amount of ice present. This analysis adopts a series addition of interstice and grain conduction after *Mellon et al.* (1997). Here,

k_w is the conductivity through the solid regolith grains and k_i is the conductivity of the interstice, which may be filled with either gas or ice. The bulk conductivity, k, is thus expressed as

$$k = \frac{k_w k_i}{(1-\phi_0)k_i + \phi_0 k_w}. \tag{6.1}$$

The ice-free porosity, ϕ_0, is assumed to be homogeneous and isotropic on length scales larger than several tens of grains. The parallel conductivity through the interstice, with contributions from gas and solid ice, is

$$k_i = (1-f_c)k_{i0} + f_c k_{\rm ice}, \tag{6.2}$$

where k_{i0} is the ice-free interstitial conductivity. The fraction of the cross-sectional area through which heat conduction occurs, f_c, was modeled by *Mellon et al.* (1997) and found to be related to the square root of the filling fraction, $f_c = (\sigma/\sigma_0)^{1/2}$; to be largely independent of grain shape; and to be completely independent of grain size at these scales. An effective grain conductivity for basaltic regolith particles of $k_w = 3.0$ W m^{-1} K^{-1}, as used by *Mellon et al.* (1997), is adopted here. Using this formulation, k is thus a rational function of the form $(A+Bf_c)/(C+Df_c)$, where A, B, C, and D are constants for a particular temperature. Thus, The thermal conductivity when the filling fraction is zero is written as $k(f_c(0)) = k_0$.

Presley and Christensen (1997) found that at atmospheric pressures appropriate for Mars, the bulk thermal conductivity in particulate media depends weakly on the absolute pressure, $k \propto p^{2/3}$, and also varies as the particle diameter as $k \propto d^{1/2}$. At 8 mbar, the range of thermal conductivities under simulated Mars conditions was found to vary from 0.011 to 0.11 W m^{-1} K^{-1} over a particle size range of 11–900 μm. Sand-sized grains composed of basaltic material were found to have $k \simeq 0.06$ W m^{-1} K^{-1}. These experimental values are similar to those used by *Mellon and Jakosky* (1995) for a general particulate regolith (0.02 W m^{-1} K^{-1}). Ice, on the other hand, has a bulk thermal conductivity of ∼2.2 W m^{-1} K^{-1} at 273 K, but as high as 3.6 W m^{-1} K^{-1} at 180 K. The conductivity of ice is given by the expression $k_{\rm ice} = 488.19/T + 0.4685$ W m^{-1} K^{-1}, which is valid in the temperature ranges of interest (*Hobbs*, 1974).

The addition of ice at grain contact points greatly increases the conductivity of the sample through increased thermal contact and conduction area attributable to preferential ice depositon as annuli at grain contact points (Chapter 5 and *Hobbs*, 1974). The parallel conductor model appropriately exhibits a rapid increase in thermal conductivity for small filling fractions. For low ice-free bulk thermal conductivities ($k_0 \simeq 0.01$ W m^{-1} K^{-1}), the value of k reaches 50% of its ice-saturated value at 10% filling. Higher ice-free values of $k_0 \simeq 1.0$ W m^{-1} K^{-1} may reach this point at only 1.5% filling. In either case, the earliest deposited ice has a significant effect on the thermal properties of the regolith.

The above scheme describing the variation in bulk thermal conductivity with ice content derives

from theoretical considerations. Data is lacking which can be used to constrain this model insofar as the data reflect changing thermal properties due to vapor-deposited interstitial ice. Investigations are currently in progress at the Mars Simulation and Ice Laboratory at Caltech to measure the dependence of k on filling fraction for a variety of materials.

6.2.3 Evolving pore geometries

6.2.3.1 *Constriction*

Three effects arising from pore ice deposition change the diffusion coefficient of the medium and thus the rate of further ice growth. First, the cross-sectional area of the pores reduces in proportion to the quantity of ice deposited. The expression

$$\phi = \phi_0 \left(1 - \frac{\sigma}{\sigma_0}\right), \tag{6.3}$$

captures the reduction of ϕ as a function of filling fraction, where ϕ_0 is the ice-free porosity and $\sigma_0 = \rho_{\rm ice}\phi_0$ represents the maximum ice content relative to free space. This parameterization was used by *Mellon and Jakosky* (1995) in modeling shallow subsurface ice growth. In Chapter 5, laboratory ice growth experiments indicated a stronger effect than that given by equation (6.3) alone. This led to the introduction of a second factor of diffusion reduction arising from a transition between Fickian and Knudsen diffusion as the pore geometry changes.

Initially, pores on the order of several tens of microns will be in the transition regime under typical Mars pressures; the mean free path of gas molecules at ∼600 Pa being within a factor of 10 of the pore diameter. The deposition of ice reduces the pore size and pushes the porous medium further toward Knudsen diffusion. In that regime, when molecule collisions with pore walls dominate the transport, one defines a chord (*i.e.,* an individual molecular "hop") as a straight line segment terminated at both ends by a pore wall. As Knudsen diffusion comes to dominate, the chord-length distribution of the pore space, l, rather than the mean free path, constrains the possible molecular trajectories. In Chapter 5, an analogous treatment to that of *Evans et al.* (1961), writes l as in equation (5.14). In this manner, the chord length is proportional to its ice-free value, l_0, and also to the porosity reduction. If the Knudsen diffusion coefficient is written as in equation (5.13), such that it depends on l and the obstruction factor ϕ/τ, as does the Fickian expression (equation (2.3)), then the combined effective diffusion coefficient (using the Bosanquet interpolation formula, equation (2.15)), can be written

$$\frac{1}{D} = \frac{1}{D_{F,0}v} + \frac{1}{D_{K,0}v^2}, \tag{6.4}$$

where $v = (1 - \sigma/\sigma_0)$ is the void fraction and $D_{F,0}$ and $D_{K,0}$ represent the ice-free values of the Fickian and Knudsen diffusion coefficients, wherein l_0 and ϕ_0 substitute for l and ϕ in equations (5.12)

and (5.13). As the filling fraction increases, v becomes smaller and the second term in equation (6.4) dominates over the first if $D_{K,0}$ is comparable in magnitude to $D_{F,0}$.

Since porosity changes with filling fraction, it is reasonable to assume that tortuosity changes as well; this being a third effect contributing to constriction. *Mellon and Jakosky* (1993) subsume all pore geometry variation into a changing ϕ; however, while ϕ changes linearly in filling fraction, τ has a different behavior. As the constricting medium approaches the limit of disconnected pores, molecules will be forced to take convoluted paths as more direct avenues are closed. Once the pore volume is no longer continuous, the tortuosity will be infinite and the gas-phase diffusivity will be zero, although empty pore volume may remain.

A variety of possible pore shape and interconnection models exist; few studies exist on which to base a robust physical relationship between tortuosity and filling fraction. The expression

$$\tau = \tau_0 \left(1 - \frac{\sigma}{\sigma_0}\right)^{-1}, \tag{6.5}$$

where τ_0 is the ice-free tortuosity, represents one simple model. Though pore spaces in a real porous medium will likely become disconnected before the filling fraction reaches σ_0, equation (6.5) has the proper values of $\tau = \tau_0$ and $\tau = \infty$ at the limits of ice-free ($\sigma = 0$) and ice-saturated ($\sigma = \sigma_0$) pore space. As appropriate for some models of pore constriction (*Zalc et al.*, 2004), equation (6.5) changes slowly at low filling fractions, rapidly increasing as complete filling is approached. Since tortuosity enters the obstruction factor of both Fickian and Knudsen diffusion coefficients, adding this expression for tortuosity into the calculations raises the exponent of v by one in both denominators of equation (6.4).

If at time $t = t_0$ the pore spaces are ice free, the Bosanquet expression is just equation (6.4) with v equal unity. At time $t > t_0$ after some ice has deposited, the ratio of equation (6.4) to the ice-free value, D_{t_0}, expresses the reduction in D as a function of $\sigma(t)$. Consider first the case where the tortuosity is independent of filling fraction (*i.e.,* τ=τ_0 for all t). If $D_{K,0} \gg D_{F,0}$, the second term in equation (6.4) is negligible and D_t/D_{t_0} will be linear in σ, giving a 50% reduction in the diffusion coefficient for 50% filling. If instead $D_{K,0} \approx D_{F,0}$, 50% filling will reduce the diffusion coefficient to less than 30% of its ice-free value, and a filling fraction of 90% would exhibit a diffusion coefficient one hundredth as large as D_{t_0}. Considering the case where tortuosity varies as the expression in equation (6.5), there is no linear dependence of D on σ. For $D_{K,0} \gg D_{F,0}$, 50% filling results in a 75% reduction over D_{t_0}, while with $D_{K,0} \approx D_{F,0}$, 50% filling gives $D_t/D_{t_0} = 14\%$.

6.2.3.2 *Choking*

Constriction restricts the flux passing into a given depth, but the reduction of pore space does not affect the saturated state of pore-space gas. An imposed barrier of low-diffusivity material, such as a

soil-free cavity in the subsurface or the top of the ice table (and its attendant phase transition), will impose discontinuities in the diffusion coefficient. But within a homogeneous, ice-bearing regolith beneath the ice table, the diffusion coefficient will change slowly as a function of position. If $\partial D/\partial z$ is indeed small, D may be taken out of the derivative in the right-hand side of equation (2.26), leaving the growth of ice at any depth in an ice-bearing region dependent on the value of the local diffusion coefficient and not its gradient. Hence, in a region with slowly and smoothly changing physical properties, ice growth at any depth is independent of the magnitude of constriction in surrounding layers. Complete filling at some depth (*i.e.,* choking) does not prevent the continued migration and redistribution of ice within unsaturated pore spaces.

These constriction effects are most strongly experienced by the shallowest stable ice, since stronger vapor density gradients experienced at the ice table relative to deeper ice produce a faster rate of ice deposition. It has been suggested (*Clifford*, 1993; *Mellon and Jakosky*, 1995) that ice deposited from vapor may completely choke off transport through these ice-rich layers. Such a condition will obtain with full saturation, when the regolith is ice-filled and no more pore spaces are available for vapor migration. Though a gradient in partial pressure still exists, the vapor flux through such a filled medium must be zero everywhere. However, an unsaturated pore space further down the mean vapor density gradient will provide a sink for the down-directed flux. If an ice-filled layer, perhaps deposited by precipitation, is introduced into the regolith column, the downward flux will erode the bottom of this layer, potentially opening up paths between the unsaturated subsurface and the atmosphere.

6.2.4 Combined effects

For a sufficiently small depth interval containing no discontinuities, the temperature gradient may be considered linear and the diffusion coefficient will be independent of depth to first order. Hence, for a constant diffusion coefficient, equation (2.26) can be written

$$\frac{\partial \sigma}{\partial t} = D\frac{18}{RT}\frac{\partial^2 p_1}{\partial z^2} \approx D\frac{18 p_1 H}{R^2 T^4}\left(\frac{H}{RT} - 2\right)^2 \left(\frac{\partial T}{\partial z}\right)^2, \tag{6.6}$$

where p_1 is the partial pressure of water vapor. The approximation above holds true for a linear temperature gradient. For a given thermal flux, the thermal gradient ($\partial T/\partial z$) is inversely proportional to thermal conductivity, k. If the instantaneous rate of ice growth in a regolith at the time deposition begins is $\partial\sigma/\partial t|_{t_0}$, and the growth rate after some time t is $\partial\sigma/\partial t|_t$, then the ratio of ice growth rates for a given vapor density gradient may be written as

$$\frac{\frac{\partial\sigma}{\partial t}\big|_t}{\frac{\partial\sigma}{\partial t}\big|_{t_0}} = \frac{D_t}{D_{t_0}}\frac{k_{t_0}^2}{k_t^2}, \tag{6.7}$$

where the identical vapor density gradients have canceled. This relationship permits comparison of relative ice deposition rates if both D_t and k_t are known functions of σ, such as were given in Sections 6.2.2 and 6.2.3.

Using the relations developed above for thermal conductivity and diffusion coefficient as functions of ice content, the reduction in deposition rate at time t relative to the initial deposition rate is shown in Figure 6.1, where $k_{t_0} = 0.05$ W m^{-1} K^{-1} and $D_{t_0} = 4.0$ cm^2 s^{-1}. This figure illustrates the extreme variation in ice growth rates which result from the initial deposition as ice enhances the conductivity of an unconsolidated medium. The solid black line and solid gray line have identical constriction parameterizations, but the gray line takes $k_t = k_{t_0}$ for all t.

The rapidly increasing thermal conductivity reduces both the thermal gradients and the ice growth rate. The thermal structure of the porous medium dominates the ice growth behavior at filling fractions below ∼25% if the thermal conductivity is allowed to vary with ice content. By approximately 1% filling fraction, the ice growth rate has been reduced by two orders of magnitude. Another order of magnitude reduction occurs by 13% filling. The reduction of D_t relative to D_{t_0} is linear in v at higher filling fractions, and the slopes of the lines in log-log space (1, 2, and 3) represent the exponent of this factor. Though thermal conductivity continues to change, it does not alter the slopes of the lines beyond about 25% filling because σ appears to the 1/2 power in both numerator and denominator of the expression for k.

6.3 Numerical Model

The growth rate of ice in pore spaces is given by equation (2.26). This equation is repeated here for ease of referral:

$$\frac{\partial \sigma}{\partial t} = -\frac{\partial J_1}{\partial z} = \frac{\partial}{\partial z}\left(D\frac{\partial \rho_1}{\partial z}\right). \tag{6.8}$$

The model uses the expressions for constriction and thermal conductivity developed in Sections 6.2.2 and 6.2.3 to determine subsurface ice growth on 100 kyr timescales. The solution of equation (6.8) may be computed efficiently because it requires only knowledge of D and temperature as functions of depth at any time. The diffusion coefficient and its gradients depend on temperature and the current filling fraction, and vapor density depends on temperature alone.

Subsurface temperatures are computable using an unconditionally stable implicit scheme. Temperature fluctuations can give rise to large variations in vapor density, particularly at the boundary between ice-bearing and ice-free soils, where the latter can experience unsaturated levels of ρ_1. The large vapor density gradients which can exist across this boundary are normally handled through explicit solution of the differential equations (as in equation (5.3)). But within the ice-bearing region, this complication may be removed if the assumption of pore-gas vapor saturation obtains at all times. The thermal diffusivity of the regolith is on the order of 10^{-8} m^2 s^{-1}, approximately

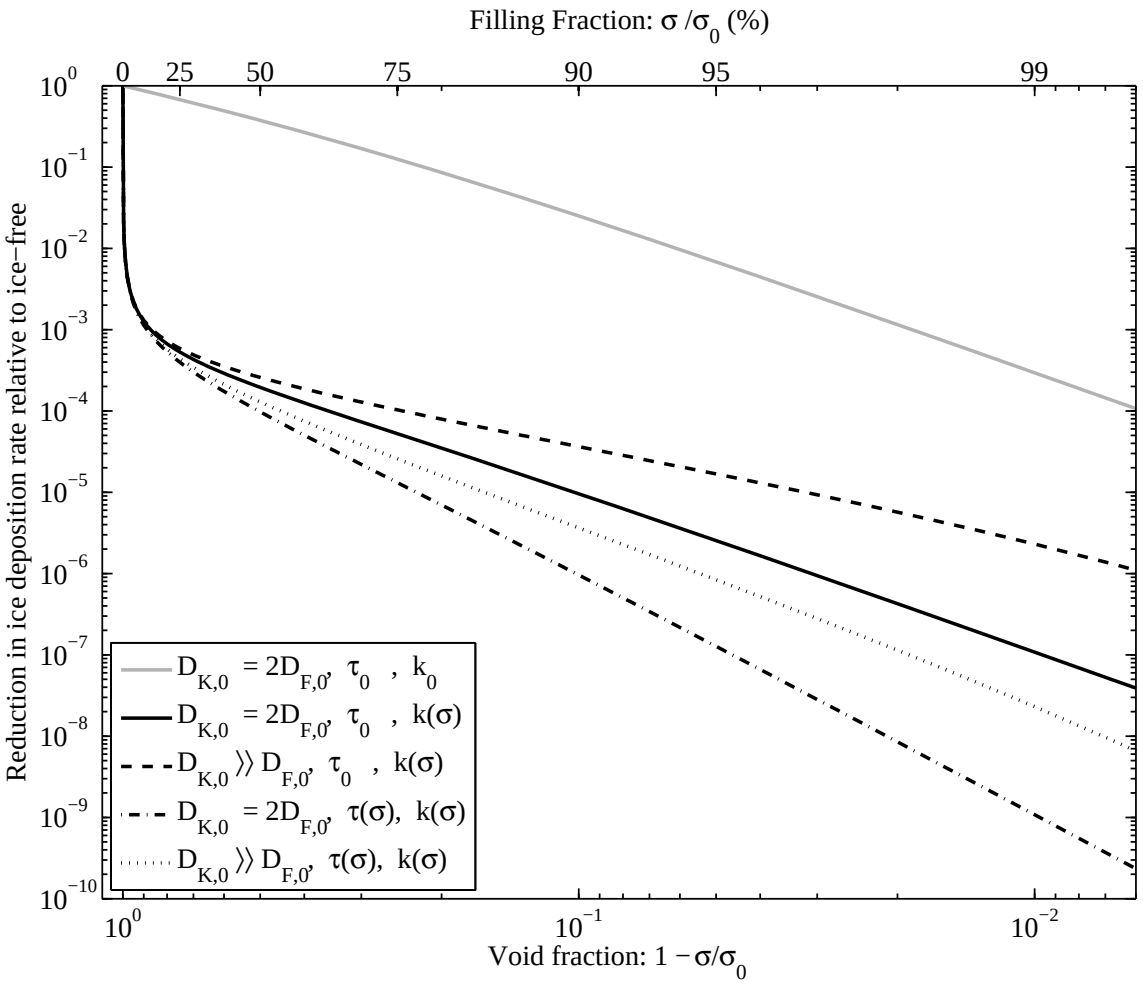

Figure 6.1: The reduction in ice deposition rate relative to the instantaneous initial deposition rate caused by constriction and thermal conductivity changes, given a constant vapor-density profile. For all curves shown, the ice-free thermal conductivity is 0.05 W m^{-1} K^{-1}. Solid lines indicate cases where tortuosity is constant with filling fraction and $D_{K,0} \approx D_{F,0}$, with $D_{F,0} = 6.0$ cm^2 s^{-1} and $D_{K,0} = 12.0$ cm^2 s^{-1}. The solid gray line excludes the effect of changing thermal conductivity. The slope of the solid lines is 2, reflecting the exponent on the dominant term in equation (6.4). The dot-dashed curve incorporates a changing tortuosity with σ and has a slope of 3. By setting $D_{K,0} =$ 1000 cm^2 s^{-1}, the second term in the expression for the effective diffusion coefficient is negligible, resulting in a model of constriction that depends on only one factor of v as in equation (6.3); this is illustrated with the dashed line (with a slope of unity).

four orders of magnitude smaller than the concentration diffusivity. Thus, the timescale for the propagation of vapor density differences is fast enough compared to the speed of the thermal wave that a timestep on the order of 10^3–10^4 seconds may be taken without violating the assumption of a vapor-saturated pore-gas. If there are no discontinuities in the diffusion coefficient within the domain of ice deposition (*i.e.,* no abrupt jumps in temperature or ice content), the growth behavior will be numerically stable with time steps on the order of several thousand seconds.

The model consists of three numerical layers. The top 0.3 m of the numerical grid resolves the

diurnal temperature wave at ∼0.9 cm intervals. This spatial resolution, coupled with the model's sub-sol timestep, provides accurate determination of surface thermal emission, which is strongly non-linear in temperature. A second grid, more coarsely spaced at ∼12.5 cm intervals, extends from the base of the diurnal region to 15 m, encompassing multiple annual skin depths. The skin depth of an ice-saturated regolith extends farther than an ice-free regolith by a factor of $\sqrt{k_1/k_0}$, where k_1 and k_0 are the bulk thermal conductivities of ice-rich and ice-free regoliths, respectively. This factor is of order 2.5 for basaltic particles with $k_0 = 0.05$ and $k_1 = 2.5$ W m^{-1} K^{-1}. The model region resolving the annual thermal wave extends to approximately ten times the skin depth of a dry regolith, and therefore encompasses ∼4–5 skin depths if the pore spaces are ice filled. Beneath this domain, a logarithmically spaced region of 50 points extends to 500 m to resolve obliquity-scale thermal oscillations.

To properly compute heat fluxes at a given location during a particular epoch, the model uses the long-term orbital element solutions for Mars computed by *Laskar et al.* (2004). These solutions provide obliquity, eccentricity, and longitude of perihelion for up to 20 Myr into Mars' past. The model computes fluxes at the surface at least ten times per sol for a given epoch, latitude, and surface albedo; timesteps may be up to 5 times smaller in cases where required by subsurface thermal properties. The surface flux includes direct and diffuse radiation using the schema of *Aharonson and Schorghofer* (2006) which assumes a diffuse IR component equal to 2% of noon insolation (*Kieffer*, 1976). The model neglects scattered radiation from atmospheric dust.

The mean annual solar insolation for the model was checked against analytical solutions given in *Ward* (1974) for polar, equatorial, and intermediate latitudes. Surface fluxes are passed to an implicit Crank-Nicolson thermal conduction scheme which propagates the temperature wave through the subsurface given thermal properties as modified by the presence of ice. If surface temperatures fall below 145 K, CO_2 deposits at the surface. The surface temperature remains fixed at the CO_2 frostpoint until the mass of accumulated CO_2 again reaches zero.

The effective bulk thermal conductivity in ice-free material, k_0, is the sum of contributions from conduction through the void space gas, conduction within the solid particles and ice, and thermal radiation between the particles. This latter contribution is usually negligible for temperatures less than 300 K. The model uses the scheme of Section 6.2.2 to compute thermal conductivity as a function of filling fraction.

The vapor pressure within the regolith is set at all points by the temperature of the ice. In cases where an ice-free surface layer is imposed, vapor densities and growth rates in this region are zero and equation (6.8) is computed for depths beneath the imposed cryosphere boundary. Similarly, an imposed ice-saturated regolith extending beneath some depth does not change with time and represents a no-flux boundary.

The diffusive properties of the ice-free regolith are assumed to be homogeneous. The diffusivities

are adjusted for every gridpoint and timestep based on temperature dependence of the Fickian ($D \propto T^{3/2}$) and Knudsen ($D \propto T^{1/2}$) regimes, as appropriate. Atmospheric pressures are assumed constant, so the P^{-1} dependence of Fickian diffusion does not play a role. The effective diffusion coefficient when the filling fraction is non-zero is computed using equation (6.4). Unless otherwise stated, the models assume an ice-free porosity of 40%.

One investigation below focuses on the relative strengths of the contributing constriction effects. By setting the ice-free Fickian and Knudsen diffusion coefficients to $D_{F,0} = 6.0$ cm^2 s^{-1} and $D_{K,0} = 12.0$ cm^2 s^{-1}, respectively, the effects of the changing pore geometry indicated by the results of Chapter 5 are employed and the effective diffusion coefficient of the ice-free medium is 4.0 cm^2 s^{-1}. This method incorporates both changing porosity and the transition to greater Knudsen diffusion contributions as the pore space constricts. To employ a constriction model equivalent to that of *Mellon and Jakosky* (1993), wherein only the porosity changes with filling fraction, the ice-free Fickian coefficient is set to $D_{F,0} = 4.0$ cm^2 s^{-1} and the ice-free Knudsen diffusion coefficient is given the unphysically large value of $D_{K,0} = 1000$ cm^2 s^{-1}. This ensures that the contribution of the Fickian term always dominates and allows the constriction parameterization to be selected at run-time given appropriate choices of ice-free diffusion coefficients. The constriction models may also include either a constant or changing tortuosity, via the relation in equation (6.5). These choices therefore bracket the range of effects attributable to the choice of constriction model. See Section 6.3.2 for a discussion of appropriate ranges for diffusion coefficients.

Having thus obtained the vapor density and the effective diffusion coefficient at all depths for a particular time, equation (6.8) gives the quantity of ice deposited in a single timestep. As a check on the model computation of ice growth rates, the accumulation of ice in early growth stages (before the diffusion coefficient was significantly altered by constriction) was compared to values computed from equation (6.8) using the diffusivity and values for the mean annual vapor density gradients computed for a perpetually ice-free regolith. The model results when ice is permitted to deposit agree well with this benchmark, with minor over-accumulation in the simple calculation being attributable to a static diffusion coefficient.

6.3.1 Model assumptions

The sub-second timesteps required to explicitly solve the vapor diffusion equation preclude running such models as those in Chapter 5 for thousands or millions of model years. Focusing on ice contents beneath the stability depth and one key assumption permits the model to be simplified and thus executed more efficiently. First, gas in close contact with ice is assumed to be saturated at all times. Gas in an ice-bearing pore equilibrates with that ice; the partial pressure of water vapor equals the vapor pressure of the ice, which in turn depends only on its temperature. This assumption is valid in circumstances where temperatures change slowly and bulk motion of the gas is negligible

(see Section 6.2.1). As discussed in Section 6.3, the concentration diffusivity is three to four orders of magnitude larger than the thermal diffusivity, allowing changes in vapor density to maintain a saturated pore space gas if the temperature fluctuations are of diurnal frequency or slower. A consequence of this assumption is that ice beneath the ice table is insulated from the vapor content of the atmosphere as discussed in Section 6.2.1.

For locations where these assumptions are valid, such as the evolution of ice perpetually beneath the ice table, they give rise to several advantages. For example, gradients which drive vapor flux within the ice-bearing regolith are independent of the atmospheric humidity, a poorly constrained quantity over long timescales. The gradients instead depend only on subsurface temperature, which is used to compute vapor densities via the Clausius-Clayperon equation and the ideal gas law. Temperature can be tracked with time-efficient implicit schemes given the surface thermal flux balance and subsurface thermal properties.

The regions of interest for the model presented here are latitudes where subsurface ice is currently stable, and depths where surface thermal fluctuations overwhelm the geothermal gradient and give rise to an inward mean-annual vapor flux. These models therefore do not include any geothermal heat flux and incorporate no subsurface vapor source; all ice which accumulates is ultimately derived from the atmosphere.

6.3.2 Model parameters: Phoenix landing site

Parameters for this model are chosen to be appropriate to the site selected for the Phoenix Mars lander; Table 6.1 summarizes these choices. The landing ellipse for Phoenix is centered on lowland bright terrain of the Scandia formation at 68.16 degrees North latitude, 233.35 degrees East longitude. The scientific rationale for selection of this region includes the presence of a near surface ice table. A variety of techniques including the gamma ray and neutron spectroscopy, ice stability theory, and TES and THEMIS seasonal temperature and thermal inertia maps indicate an ice rich layer beneath between 2–6 cm of ice-free soil (1–9 cm, including uncertainties) (*Mellon et al.*, 2008). The spectrometry calculations assume a dry soil density of 1600 kg m^{-3}. This depth allows the possibility that both the ice table and a region of ice-free soil will be within reach of Phoenix's robot arm. The thermal inertia for ice free soil in this region is expected to be $\sim$250 J m^{-2} K^{-1} $s^{-1/2}$ (*Putzig et al.*, 2005; *Putzig et al.*, 2006). The bulk thermal conductivity chosen to represent dry particulate basaltic regolith (0.05 W m^{-1} K^1) falls close to the value of 0.06 given by *Presley and Christensen* (1997) for medium-sand-sized particles. This is slightly higher than the value of 0.02 W m^{-1} K^1 used by *Mellon and Jakosky* (1993). The albedo of the landing site region is approximately 0.28 (*Paige et al.*, 1994; *Putzig et al.*, 2006). The range of atmospheric pressure experienced at the landing site region ranges from 700–1100 Pa (*Tamppari et al.*, 2008), and a constant value in the middle of this range, 900 Pa, is chosen for use in the model.

The porosity of the ice-free soil at this site is unknown, so a mid-range value of 40%, typical of medium-sand-sized material, is chosen. Variation of porosity over a wide range of 20–70% is shown to have a minor effect on the ice density profiles which develop. The ice-free diffusivity is also a poorly constrained quantity for Mars surface materials. Previous work described in Chapter 2 and the investigations of Chapters 3 and 4 suggest that a value in the range of 2–6 $cm^2\ s^{-1}$ is appropriate. An effective diffusivity of 4.0 $cm^2\ s^{-1}$ is obtained using 6.0 and 12.0 $cm^2\ s^{-1}$ as values for the ice-free Fickian and Knudsen diffusivities. The individual ice-free diffusion coefficients are also within a plausible range and are similar to the results obtained in Section 3.5.1.2, where these two quantities were determined for 50–80 μm glass beads.

Parameter	Value	Reference
Latitude	68°	*Arvidson et al.* (2008)
Albedo	0.28	*Paige et al.* (1994); *Putzig et al.* (2006)
Pressure	900 Pa	*Tamppari et al.* (2008)
k_0	0.05 W m^{-1} K^1	*Presley and Christensen* (1997)
Thermal inertia	250 J m^{-2} K^{-1} $s^{-1/2}$	*Putzig et al.* (2006); *Mellon et al.* (2008)
Regolith bulk density	1600 kg m^{-3}	*Boynton et al.* (2002); *Feldman et al.* (2002)
Ice-free diffusivity	4 $cm^2\ s^{-1}$	*Hudson et al.* (2007); *Hudson and Aharonson* (2008)
Ice table depth	2–6 cm (1–100 cm)	*Mellon et al.* (2008)
Ice-free porosity	40% (20–70%)	*Hudson et al.* (2007) and references therein[1]

Table 6.1: Model parameters; chosen for similarity to Phoenix landing site. Values in parentheses represent the range of values examined in various model runs. [1] No data on soil porosities at the Phoenix landing site are currently available; the range and nominal value given is based on laboratory simulants and terrestrial sand-sized soils.

Both ice-free soil at the surface and a massive sheet of ice-cemented soil at some depth will perturb the thermal profile, thereby affecting the rate of ice growth in unsaturated pore spaces. The history of subsurface ice over 5 million years of recent Mars history was examined in *Schorghofer* (2007). It was shown that numerous retreat events would have depleted a initial massive ice sheet deposited during earlier epochs via precipitation. The retreat of the ice sheet, which was assumed to include some quantity of soil particles, resulted in the formation of a porous lag deposit. This deposit would, during favorable epochs, experience interstitial ice deposition via diffusive processes. For a climate which favors ice loss to remove mass from the ice table, it would first need to remove all of the pore ice in the above regolith.

Three retreat events of sufficient strength and duration to do so have occurred between 600–300 ky ago; however, the quiescent obliquity history of the past 300 ky have not been conducive to ice loss events of comparable magnitude. The models discussed below begin 300,000 years ago, after the last substantial ice-loss event.

The initial conditions for all models include some depth of ice-free regolith. The depth to the shallowest stable ice, the ice table, is manually set for each model run. To illuminate the effect of a massive subsurface ice sheet, some models are run with pore-filling ice which extends from some

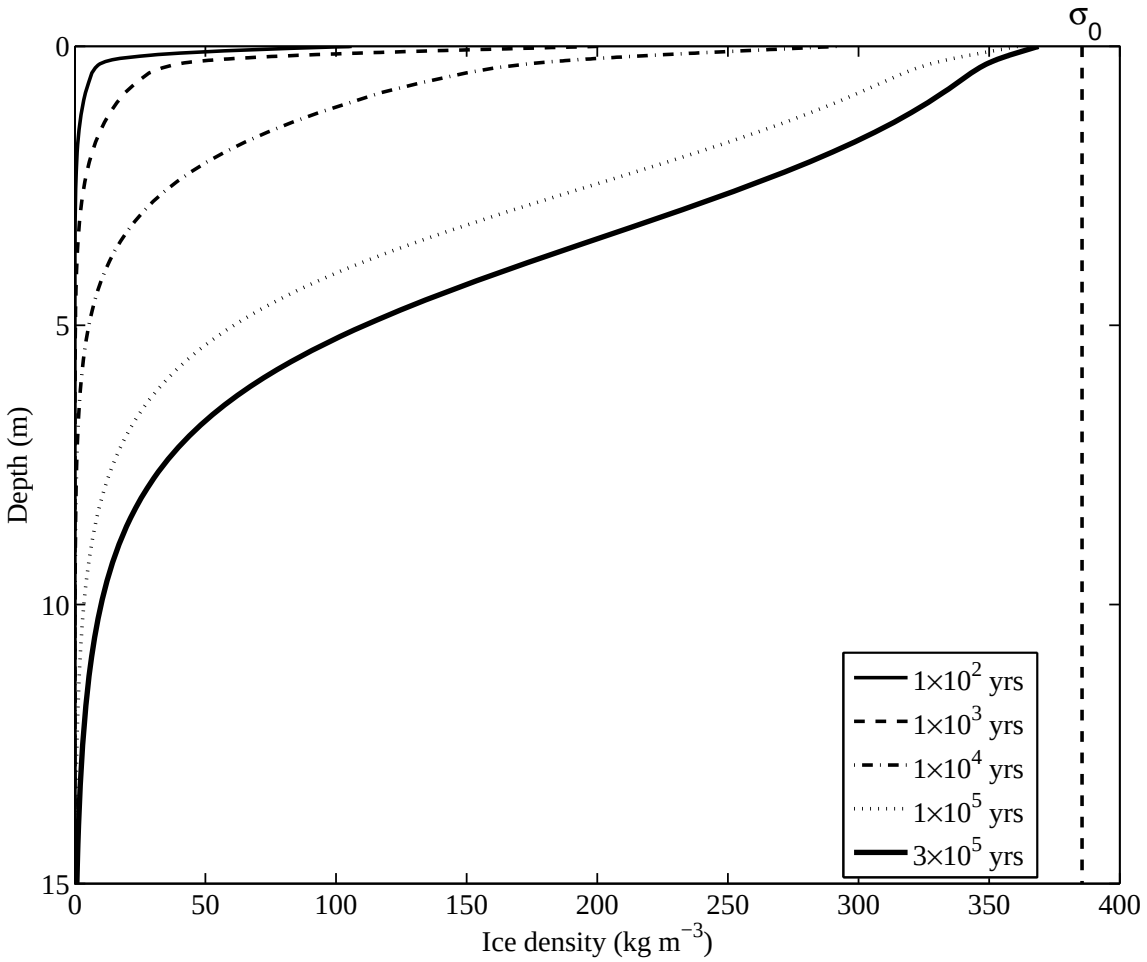

Figure 6.2: Logarithmically spaced time intervals of modeled pore-ice growth from 10 to 100,000 years; the final model profile at 300,000 years is also shown. The constriction model uses $D_{F,0} = 6.0$ and $D_{K,0} = 12.0$ (in cm^2 s^{-1}) and a constant τ. High temperature gradients in shallow depths give rise to high filling fractions in short time intervals, creating a sharp bend in the early profiles. Increasing thermal conductivity of shallow layers as ice deposits results in higher gradients and growth rates at depth, thereby smoothing the profiles with time.

shallow depth down to the bottom of the model domain. These models do not simulate minor ice-loss events which may have penetrated to depths shallower than the massive ice sheet in the last 300 ky, but instead assume conditions favorable to ice deposition below the ice table depth for the entire time interval. Therefore, these results represent an upper bound on the quantity of ice, deposited since 300 kya, which may exist in the subsurface.

6.4 Results

A profile of ice content as a function of depth at logarithmically spaced time intervals is given in Figure 6.2. These profiles are for a single model begun with an initially ice-free regolith and allowed

to evolve for the most recent 300,000 years of Mars' orbital history; ice stability was assumed for all depths. The model uses a constriction parameterization wherein the ice-free Knudsen diffusion coefficient is comparable to the Fickian diffusion coefficient ($D_{F,0} = 6.0$ cm^2 s^{-1} and $D_{K,0} = 12.0$ cm^2 s^{-1}), and τ does not vary with filling fraction.

This figure shows that ice growth is most rapid in the shallowest layers, with the surface reaching 27% filling in 100 years and 52% filling in 10,000 years. This rapid growth arises from the high thermal gradients, producing in turn high vapor density gradients, permitting the rapid deposition of ice. The deposition rate is reduced as the effect of constriction becomes stronger. In the first 100,000 years of growth, the surface layer accumulates enough ice to fill 94% of the available pore space. In the last 200,000 years, however, the ice content of the surface layer grows by only 2%, reaching 96% filling, despite the obliquity exhibiting a similar amplitude over the entire modeled time interval.

As ice accumulates in the shallow subsurface, the thermal conductivity of ice-bearing layers increases. This has two effects: First, the gradients in the shallowest layers are reduced, further contributing, along with constriction, to the reduction in shallow ice growth rate. Second, greater quantities of heat are conducted to depth, permitting larger gradients there and enhancing ice deposition. These effects smooth out the ice content profile, which initially exhibits a sharp bend at approximately 0.2 m depth for times less than 1,000 years. If conditions favorable to ice deposition persist, the profile will continue to accumulate ice, with all depths approaching the maximum possible filing, σ_0. The base of the cryosphere is indistinct as ice content reduces slowly toward zero with increasing depth. Though not shown here, the annual thermal wave will be overwhelmed by the geothermal gradient at approximately 10–20 m and this may affect the profile at these depths.

6.4.1 Constriction effect on ice growth

The ice contents following 300,000 years of accumulation for various constriction models are presented in Figure 6.3a. The diffusion parameters are chosen such that at zero ice content, the effective diffusion coefficients of the models are the same: for a case where the ice-free Fickian and Knudsen diffusion coefficients are comparable in magnitude, $D_{F,0} = 6.0$, $D_{K,0} = 12.0$. When $D_{K,0} \gg D_{F,0}$, then $D_{F,0} = 4.0$ and $D_{K,0} = 1000$ (vaules are in cm^2 s^{-1}). Ice stability is assumed at all depths.

Overall, there is only a moderate difference between the models following 300 kyr of accumulation as displayed in Figure 6.3a. Initially, the ice growth rates of all models are comparable since the initial ice-free diffusion coefficients are identical. Only after some significant quantity of ice deposits do the differences in constriction parameterization come to dominate the further evolution. For example, in Figure 6.3a, the strongest and weakest constriction models bracked the intermediate cases for depths where the accumulation has become greater than ∼25–40% (*e.g.,* for depths shallower than ∼4 m). The weakest parameterization uses a constant τ and $D_{K,0} \gg D_{F,0}$, such that constriction

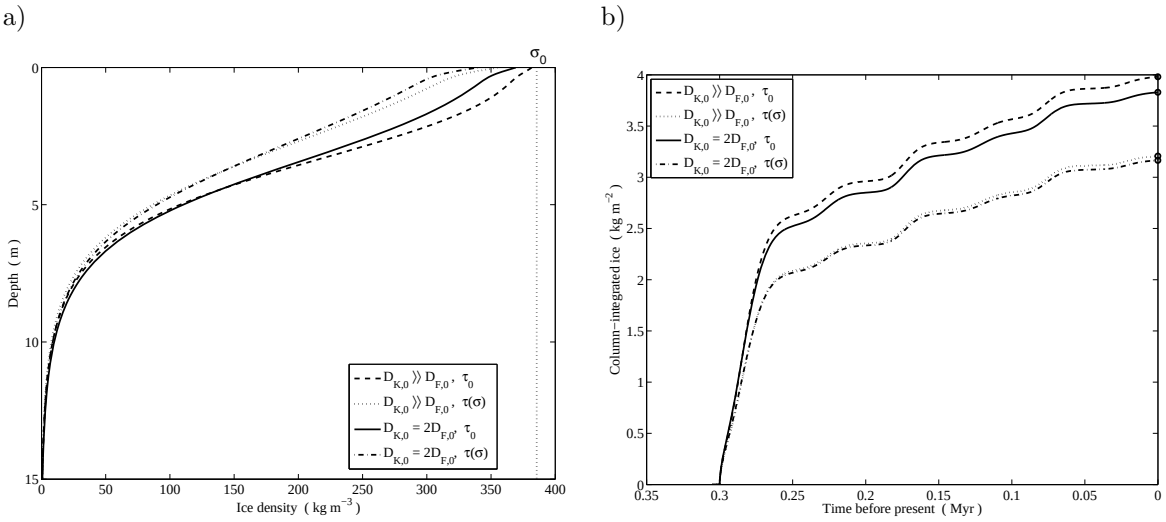

Figure 6.3: These plots compare a) ice content profiles as a function of depth and b) column-integrated ice contents as a function of time for models incorporating various parameterizations of constriction. Plot a) shows the final ice contents following 300,000 years of ice growth. The ice-free diffusion coefficients when $D_{K,0} \gg D_{F,0}$ are (in cm^2 s^{-1}): $D_{F,0} = 4.0$, $D_{K,0} = 1000$; otherwise $D_{F,0} = 6.0$, and $D_{K,0} = 12.0$. A constant tortuosity is indicated by τ_0, while $\tau(\sigma)$ denotes tortuosity varying according to equation (6.5). The weakest (dashed line) and strongest (dash-dotted line) constriction models bracket the others following sufficient profile evolution for differences in constriction to become apparent. The weakest constriction model reaches within 1% of complete filling at the surface in 300 kyr. In b) the total quantity of ice accumulated differs by less than 50% between the strongest and weakest constriction models at 300 kyr, and that most of the difference among models arises from different parameterizations of τ. All models presented here assume ice stability at all depths.

is entirely due to changes in ϕ (as in equation (6.3)). Such a model reaches 99.0% pore filling at the surface in 300,000 years. In contrast, the surface filling fraction for the strongest constriction model, incorporating a variable τ and $D_{K,0} \approx D_{F,0}$, attains only 88.1% in the same interval.

Figure 6.3b compares the column-integrated ice contents for various constriction models as a function of time. The ice content below ∼15 m is approximately zero, so these column-integrated values essentially trace only the evolution in the upper 15 m of the regolith. All exhibit a rapid increase in ice content early in the deposition phase due to high temperatures and the resulting high vapor density gradients at the surface. After approximately 20,000 years, the accumulation rates decrease sharply and the models diverge as the weaker constriction parameterizations permit more ice to deposit. After ice growth has progressed for 300,000 years, the column integrated ice contents differ by at most 50%. Yet most of this difference is due to the choice in τ parameterization. If one particular model for tortuosity is selected, the difference between column ice contents for $D_{K,0} \approx D_{F,0}$ versus $D_{K,0} \gg D_{F,0}$ is less than 5%.

Figure 6.4 contains the same model data as Figure 6.3, but displays the difference in ice content relative to a comparison case for two particular depths. The comparison case is chosen to be the

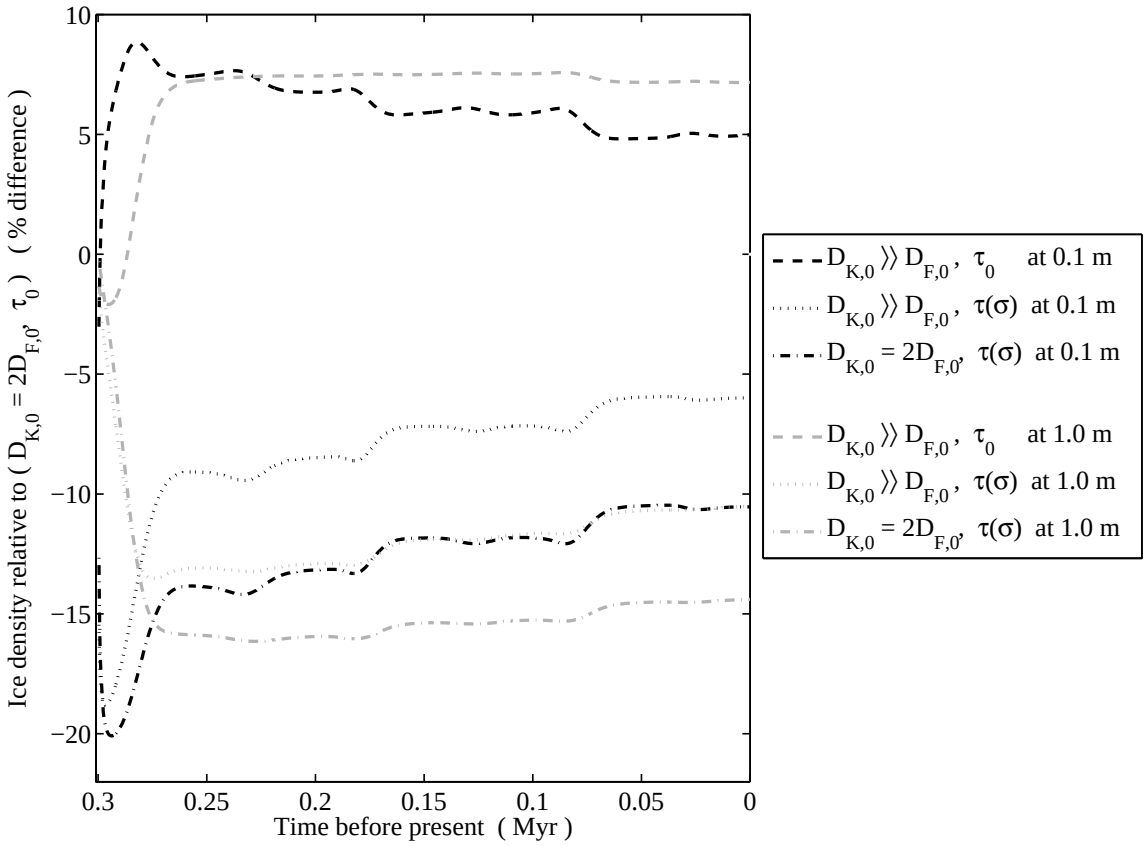

Figure 6.4: This figure plots, as a function of time, the difference in ice content between the constriction model that employs both constant tortuosity and $D_{K,0} = 2D_{F,0}$, and the other three models presented. The black lines represent the difference at 0.1 m depth; the gray lines 1.0 m. The models with constant τ (dashed lines) accumulate more ice than the comparison model at these depths and exhibit between 5–10% more ice for most of the modeled time interval. Variable τ models accumulate less ice than the comparison model, differing by as much as 20%. The maximum differences (at early times) are more exaggerated for shallower depths where accumulation can occur the fastest; for the same reason, these depths also converge toward zero difference faster than deeper levels. The slow approach of all models to the comparison case reflects the long times requried to reach the ultimate end-state of a completely filled regolith.

model incorporating constant tortuosity, $D_{K,0} = 12.0$ cm^2 s^{-1}, and $D_{F,0} = 6.0$ cm^2 s^{-1} (*i.e.,* the solid lines in Figure 6.3). Black lines in Figure 6.4 show relative ice contents at 0.1 m and gray lines show relative contents at 1.0 m. After long times, all regolith depths approach 100% filling and the difference between cases will become zero.

The constriction model that is weaker than the comparison case, *i.e.,* the one which incorporates only changes in ϕ to account for reduced diffusion coefficients, exhibits an overall higher ice content than the comparison model at a given time. The initial divergence at shallow depths is fast, occuring within the first 20,000 years, and is followed by a slow convergence toward the comparison case. Models which incorporate a changing τ are more strongly constricted than the comparison case and exhibit negative relative ice contents. The higher constriction experienced by these models results in

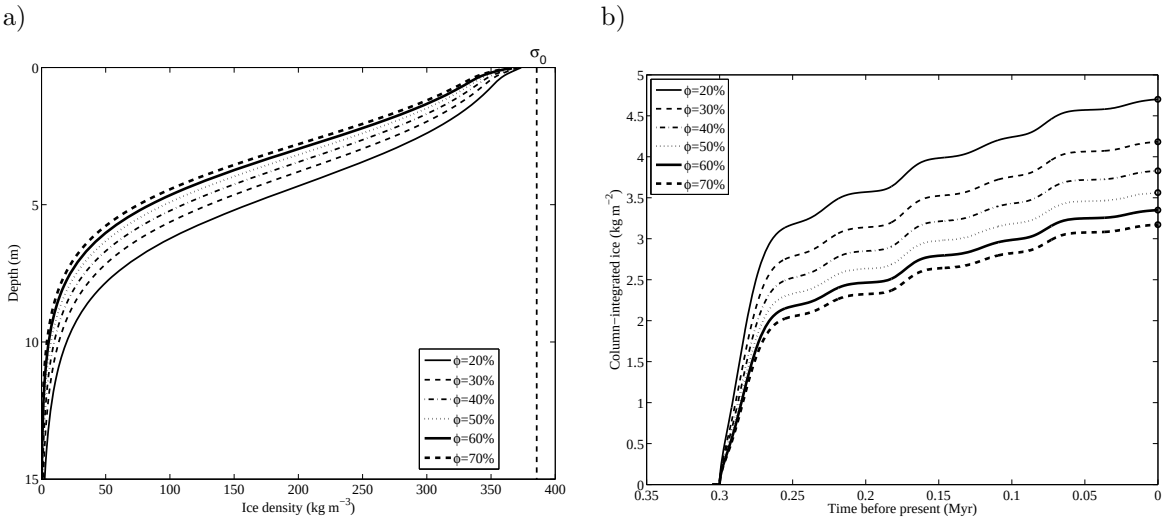

Figure 6.5: Models with identical constriction parameterizations are run with different ice-free porosities assuming ice stability at all depths. The value of τ is constant and $D_{F,0}$ and $D_{K,0}$ are 6.0 and 12.0 cm^2 s^{-1}, respectively. The divergence among these models is of the same order as that arising from different constriction models (compare Figure 6.3). Surface ice contents are only ∼6% different between 20% and 70% porosity cases. The variation in column ice contents seen in b) is less than 40% after 300,000 years of ice accumulation.

their slower convergence back to the comparison case compared to the weaker constriction models. Also, the stronger constriction models diverge more sharply from the comparison case than the weaker model, exhibiting a maximum relative density difference of 20% versus 10%.

High thermal gradients in the shallow subsurface produce the fastest growth rates. This explains the divergence from and re-convergence to the comparison case being most rapid for near-surface soils. The deeper soils generally exhibit a subdued trend compared to shallower soils, lacking the large early divergence peak and experiencing slower convergence to the filled state.

6.4.2 Porosity

Figure 6.5 displays the model outputs using a range of values of ice-free porosity from 20–70%. The constriction parameterization for all these models employs constant τ, $D_{F,0}$ = 6.0 cm^2 s^{-1} and $D_{K,0}$ = 12.0 cm^2 s^{-1}; ice stability is assumed for all depths. The differences among the ice content profiles in Figure 6.5a is smaller in magnitude than that seen among the constriction models in Figure 6.3. The range in ice contents for near-surface layers after 300 kyr are 86–91% of total filling. Comparing column-integrated ice contents among models with different porosities (Figure 6.5b exhibits differences of at most 40% following 300,000 years of ice accumulation. This degree of variation is similar in magnitude to that arising from various constriction models.

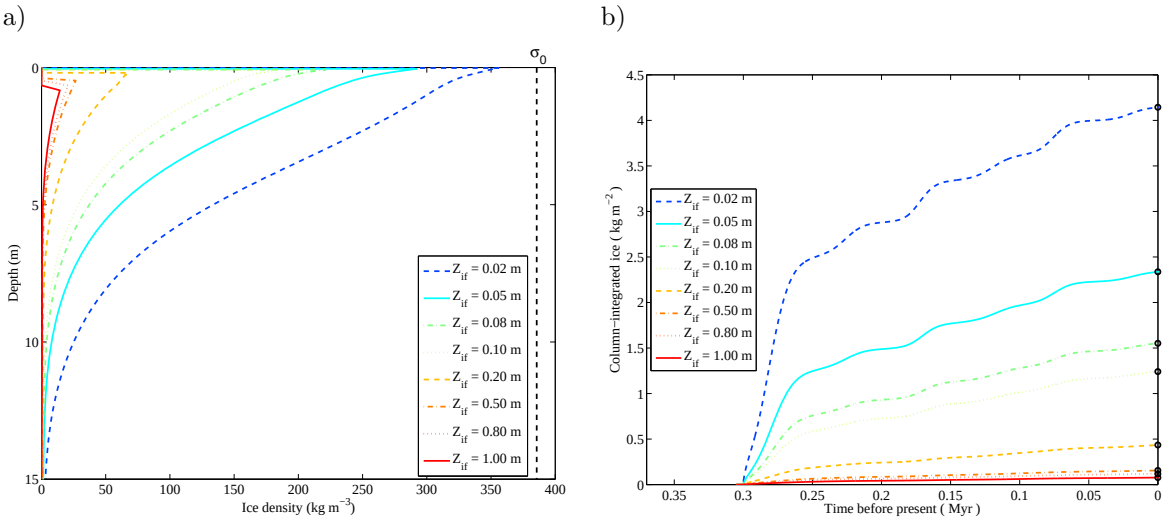

Figure 6.6: These figures show the results of models run with identical constriction parameterizations ($D_{F,0} = 6.0$ cm^2 s^{-1}, $D_{K,0} = 12.0$ cm^2 s^{-1}, constant τ), but different thicknesses of ice-free surface layers ($Z_{\rm if}$). In cases where ice grows near the surface, the high temperature fluctuations give rise to greater quantities of deposited ice. This ice, in turn, conducts surface heat to depth with greater efficiency than dry regolith, resulting in increased gradients at depth and a more ice-rich column than more insulated cases. The depth of the shallowest ice affects the quantity of subsurface ice growth much more strongly than the effect arising from different constriction parameterizations.

6.4.3 Ice-free layer

For this and all subsequent models, unless otherwise indicated, the constriction parameterization used employs $D_{F,0} = 6.0$ cm^2 s^{-1}, $D_{K,0} = 12.0$ cm^2 s^{-1}, and constant $\tau = \tau_0$.

Figure 6.6 displays the ice content profiles and column-integrated ice contents for 9 models run with different thicknesses of perpetually ice-free surface layers. The range of ice-free layer thicknesses, $Z_{\rm if} = 0.01$–1.0 m, reflects the range of ice-table stability depths experienced by mid- to high-latitude regions on Mars under the present climate (*Mellon et al.*, 2004).

Ice accumulation is greatly subdued by small increases in ice-free layer thickness. At a depth of 1 m, the model employing $Z_{\rm if} = 1$ cm accumulates more than 10 times as much ice as the model where $Z_{\rm if} = 1$ m. The difference in column-integrated ice content is even larger, being approximately two orders of magnitude between the cases with 1 cm and 1 m ice tables.

6.4.4 Deep ice

If conditions favorable to precipitation existed prior to ∼5 million years ago, a massive ice sheet may still exist below some depth at high latitudes (*Schorghofer*, 2007). The effect of this ice will be to impose perturbations on the subsurface temperature field and to present a shallow no-flux boundary to diffusive transport. In the model discused here, such a massive ice sheet is represented by pore ice with a 100% filling fraction, the difference in thermal conductivity between pure ice and ice-filled

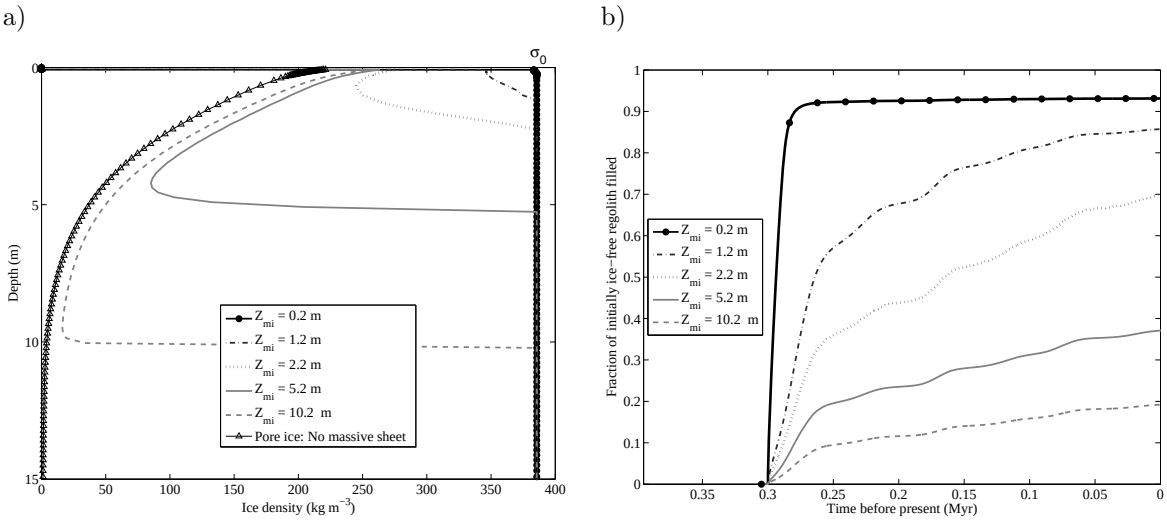

Figure 6.7: Models with identical constriction parameterizations ($D_{F,0}$ = 6.0 cm^2 s^{-1}, $D_{K,0}$ = 12.0 cm^2 s^{-1}, constant τ) are run with initial massive ice sheets extending for various depths ($Z_{\rm mi}$) to the bottom of the model domain. Each model is run with an 8 cm ice free surface layer. Rather than column-integrated ice contents, panel b) plots the fraction of initially available pore space that has filled as a function of time. Shallow regoliths fill more quickly than deeper regoliths, both due to smaller available volumes and higher thermal (and therefore vapor density) gradients.

regolith being only ∼10%.

Figure 6.7 presents plots of the ice contents for a series of models run with pore-filling massive ice sheets extending from some depth ($Z_{\rm mi}$) to the base of the model domain. Each model has an ice-free regolith layer 8 cm thick above the ice-stability depth. Panel a shows the ice content profiles for each model with a deep ice layer. For comparison, a model from Figure 6.3 with the same constriction parameters (solid black line in that figure) and without any initial pore ice is also shown (solid line with triangular gridpoints).

In Figure 6.7b, rather than column-integrated ice contents which would be skewed by the presence of the initial pore-filling ice, the curves represent the fraction of initially available regolith pore space which has become filled as a function of time. The model designated $Z_{\rm mi}$ = 0.2 m, has a massive ice sheet extending from 0.2–500 m, and an ice-free layer between the surface and 8 cm. This small initially ice-free volume fills rapidly, approaching within 1% of total filling by 60,000 years. Constriction is strong when ice contents are so high, and even though this model does not incorporate a changing tortuosity, the effects of porosity reduction and increased Knudsen diffusion reduce the ice accumulation rate to almost zero.

To explicitly examine the variation in ice content at particular depths as a function of $Z_{\rm mi}$, Figure 6.8 plots the difference in ice content ($\delta\sigma$), relative to a model with no massive ice sheet (the solid black curve in Figure 6.3 a), for depths of 0.1 and 1.0 m. The gray lines, which plot variation at 1.0 m depth, are not plotted for $Z_{\rm mi}$ = 0.2 and 0.8 meters. At all times and depths, the models

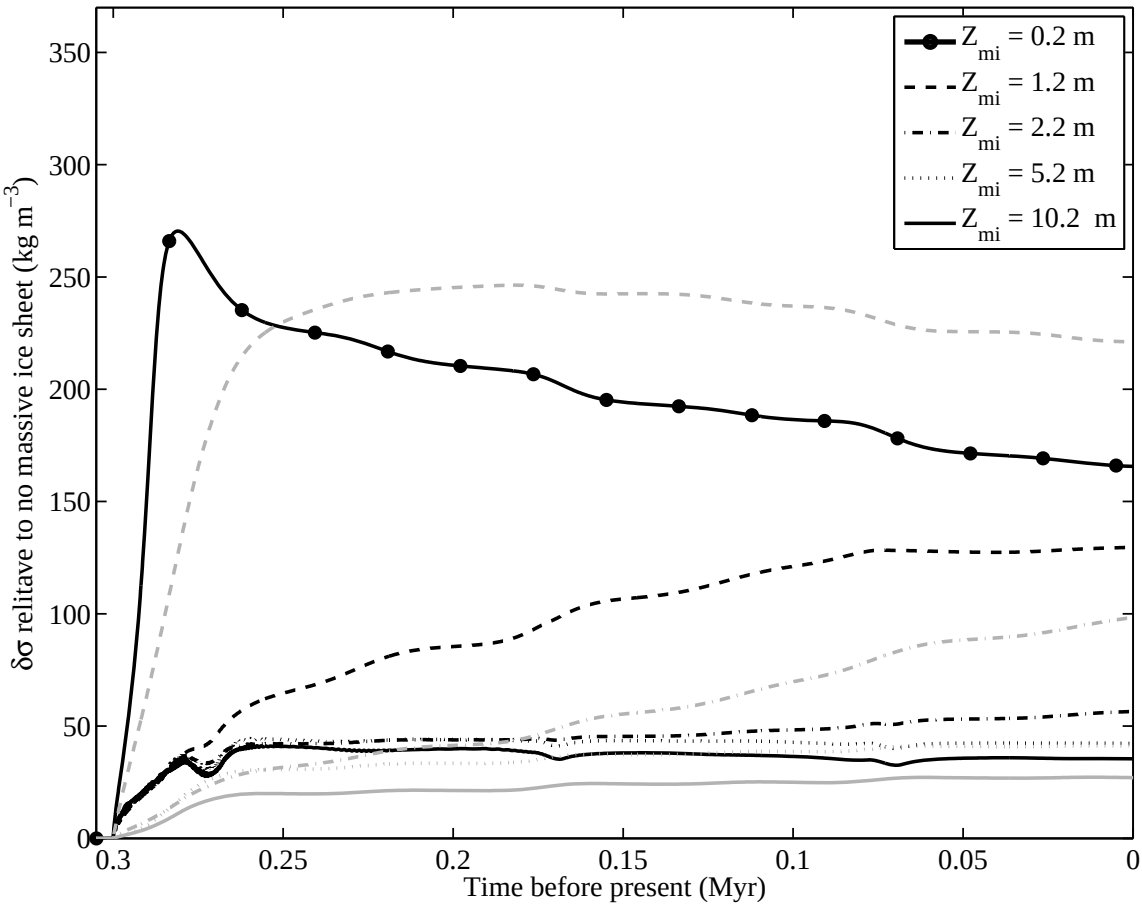

Figure 6.8: The same data as in Figure 6.7, plotted as the quantity of ice accumulated at various depths (black for 0.1 m, gray for 1.0 m) relative to a model with no massive ice sheet (*i.e.,* the solid black line in Figures 6.3 a) and 6.7 a). The cases where $Z_{\mathrm{mi}} = 0.2$ and 0.8 m are not plotted for 1.0 m depth (gray).

exhibit an increased ice content relative to a model with no ice sheet. The ice sheet significantly increases the heat capacity of the regolith and so reduces the temperature fluctuations at the base of the ice accumulation region. This compresses the thermal gradients in this region, resulting in higher driving forces for ice accumulation at all depths.

The deviation is minor for depths which are both far from the ice table and the massive ice sheet. An interesting effect is the enhanced deposition at the base of the accumulation region close to the massive ice sheet. This effect is seen as the change in direction of ice content profiles in Figure 6.7a, where they smoothly approach 100% filling near their respective massive ice sheets. For example, the grey dash-dotted line represents accumulation at 1.0 m depth for a case where a massive ice sheet exists below 1.2 m. At such proximity to the ice table, significantly more ice accumulates relative to the case without a massive ice sheet. This is despite the initial profiles having a sharp jump from ice-free to ice-full at these depths.

The two effects of altered temperature profiles and no-flux boundaries result in an enhanced deposition of ice at all depths when a massive ice sheet is present, compared to porous soil exhibiting no such massive ice. Presumably, the same effect would occur if the massive sheet were replaced by solid rock, since the rock would also exhibit higher thermal conductivity and prevent the flux of vapor. The magnitude of the effect, however, may be different due to the difference in heat capacity of rock versus ice.

6.5 Discussion

The model code in Chapter 5 explicitly solves the complete diffusion equation and requires several days of computer time to simulate ice deposition over a one-week interval. The innovative technique used in this chapter requires that gradients in vapor density arising from temperature variations propagate fast enough relative to the model timestep that pore-gas saturation is maintained. This requires that the model examine only regions where ice is present; it therefore does not include the ice table and does not compute equilibrium ice table depths. This modeling scheme is more than seven orders of magnitude faster than that employing equation (5.7), permitting the accumulation of subsurface ice to be tracked for many obliquity cycles with similar computational expense to the models of Chapter 5.

In the foregoing model results, the effect of a number of parameters on subsurface ice content were examined. By far the most influential of these, both with respect to the quantity of near-surface ice and to the total amount of ice accumulated in the regolith column, is the thickness of the ice-free layer at the surface. The low thermal inertia of the dry regolith layers rapidly attenuates the extreme diurnal temperature fluctuations, thus the maximum temperatures and temperature gradients experienced by deeper ice tables are significantly reduced relative to shallower ice. The vapor density gradients driving ice deposition are likewise lower.

For the Phoenix landing site, where the ice table is predicted to be within 2–6 cm of the surface, models here indicate that 300 kyr would allow between 70% (for $Z_{\mathrm{if}} = 6$ cm) and 92% (for $Z_{\mathrm{if}} = 2$ cm) of the pore spaces at the top of the ice table to become filled. Figure 6.9 shows these ice contents in the upper 0.5 m of the regolith as predicted by the model for values of Z_{if} between 2 and 10 cm. If the depth to ice stability is more than $\sim$2 cm, conditions at the Phonenix landing site will not have produced a completely ice-filled regolith since a major ice-loss event 300 kya. As the depth to the ice table increases, the total quantity of ice deposited in a given time interval is reduced.

The ice-free layer thicknesses assigned in the models do not change over the 300 kyr interval considered. However, Mars' climate during this time, though perhaps more stable than in periods with higher amplitude obliquity oscillations, has doubtless experienced some fluctuation in mean annual atmospheric water content, shifting the equilibrium ice table position. Ice loss events which

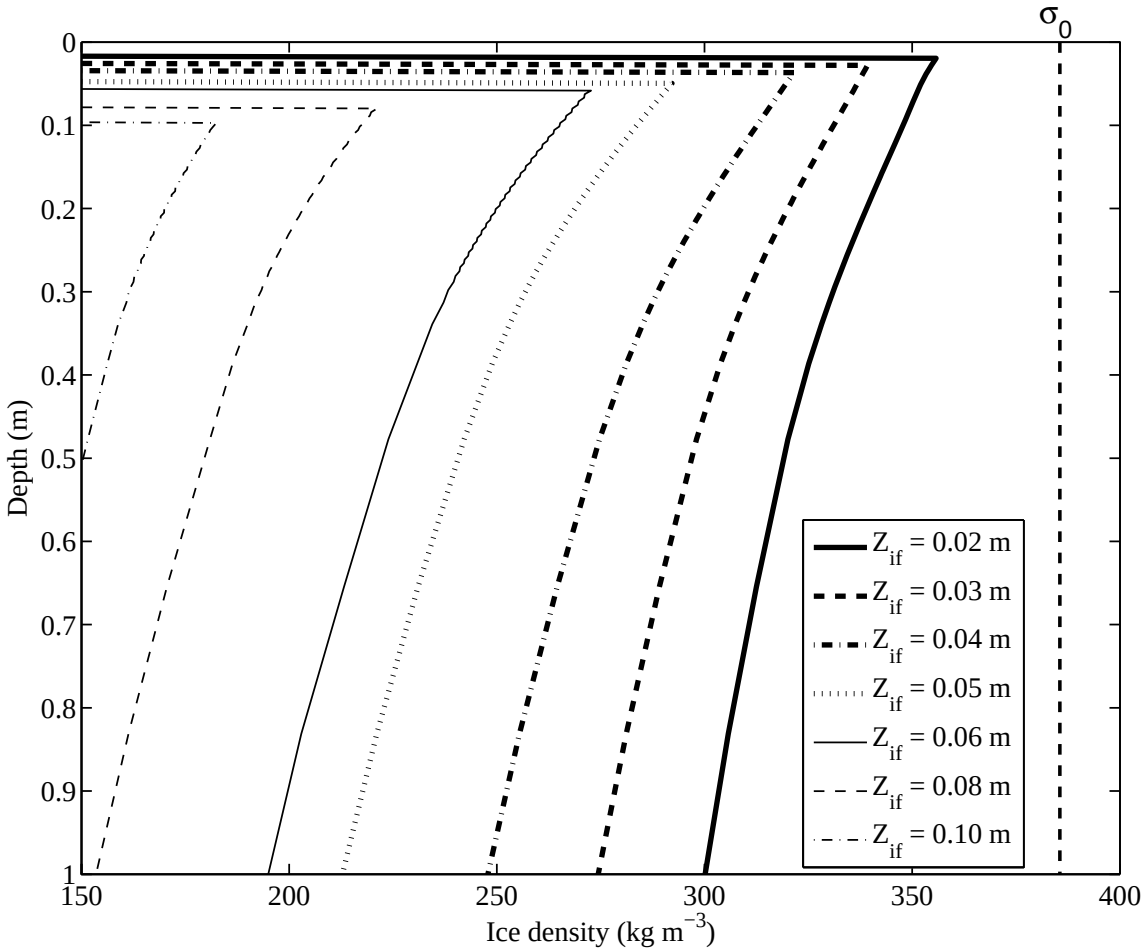

Figure 6.9: This figure presents ice content profiles of near-surface layers as in Figure 6.6 a), with additional values of $Z_{\rm if}$ shown. In cases where ice grows near the surface, the high temperature fluctuations give rise to greater quantities of deposited ice. This ice, in turn, conducts heat to depth with greater efficiency than dry regolith, resulting in a more ice-rich column than in cases where ice deposits only at deeper levels. A change of $Z_{\rm if}$ from 2.0 to 6.0 cm results in a decrease in filling fraction at the ice table from 92% to 70%. The depth of the shallowest ice affects the quantity of subsurface ice growth much more strongly than the effect arising from different constriction parameterizations.

have desiccated the porous regolith down to some depth will partially reset the ice accumulation in shallow layers. Ice which remains below the lowest depth of penetration of the ice table will affect subsequent accumulation through both its effect on the thermal structure of the regolith and the lower diffusion coefficient in the ice-bearing region.

As revealed in Figure 6.7a, and in Figure 6.8, the presence of a massive ice sheet results, for all depths and time intervals, in ice contents being greater than those accumulated when no ice sheet is present. When an ice-saturated sheet exists, the ice content at a depths near the sheet are significantly enhanced over the initially ice-free regolith. This effect arises from the no-flux condition

imposed by the massive ice sheet. Vapor is unable to move through the ice sheet and cannot move against the mean annual vapor density gradient. The local vapor density is thus increased above the saturation point and ice deposits against the ice sheet. Ice profiles developed in initially ice-free pore spaces in the presence of a massive ice sheet therefore exhibit a local minimum in ice content at some depth, rather than a monotonic decrease to the ice sheet boundary. Such inflections may be observable in high-resolution subsurface ice measurement techniques such as coring.

The ice-age dynamics model of *Schorghofer* (2007) predicts that a massive ice sheet which initially extended to the surface 5 million years ago would have been forced to retreat by periods of climate conducive to ice loss. The amount by which the ice sheet is predicted to have retreated would give rise to an approximately 40-cm-thick porous lag if the initial ice sheet contained ∼15% regolith material. If the depth to the present-day massive ice sheet were close to this value, and conditions had been favorible to subsurface ice growth beneath 8 cm for the last 300 kyr, then the regolith would be almost completely ice-filled and the current ice profile would fall between the dash-dotted line of Figure 6.7a and a condition of nearly complete filling at all depths.

Besides massive ice sheet depth and ice-free surface layer thickness, the other effects considered were seen to have minor effects on the ice content profiles. If the pore geometry were changed in such a way as to retain the ice-free diffusion coefficient at 4.0 cm^2 s^{-1}, but ice free porosity were varied between 20 and 70%, at most a 40% change in column-integrated ice content would result. A real material, however, would exhibit simultaneous changes in ϕ, $D_{F,0}$, and $D_{K,0}$. Such combined effects are not explored here.

Constriction was also observed to have a comparatively minor effect on ice content profiles. The various models employed result in an approximately 50% difference in total accumulated ice content in 300 kyr, but only a 10% difference in pore filling at the surface. This is a small variation compared to changing the ice-free layer thickness by ∼1 m, which results in two orders of magnitude difference in column integrated ice. The small differences in surface ice content among various constriction models, though easily measurable in a laboratory, may be difficult to detect *in situ*. Between the models with the strongest and the weakest constriction parameterizations, there is no more than a ∼20% difference in ice content which could be observed. It is therefore unlikely that investigations by the Phoenix lander will discriminate among the constriction models presented here; further theoretical and laboratory investigations will be necessary to make an informed choice of constriction model.

At any given site of ice accumulation and long-term stability, both the models included here and those of previous investigations (*Mellon and Jakosky*, 1995; *Schorghofer and Aharonson*, 2005) indicate that the site of greatest ice accumulation will be the local equilibrium depth. Future investigations which probe subsurface ice contents, either via indirect sensing techniques such as ground-penetrating radar or directly through drilling and coring activities, will likely encounter the

highest water contents at the ice table. The pore ice concentration will be reduced with increasing depth, though the change may be only 10–15% over distances on the order of 0.5 m (see Figure 6.9). A smaller degree of reduction in ice content with depth would be expected if the ice had been accumulating for longer than 300 kyr and thus had been able to approach total filling over a significant depth range. Such a distribution would indicate that climate changes inducing ice loss have not been of sufficient magnitude or duration to penetrate and reset the ice contents over these depths.

Figure 6.10 shows the difference in mean annual surface temperatures resulting for various distributions of subsurface ice. An ice-filled regolith (excepting an 8 cm ice-free surface layer) exhibits a 10 K temperature difference relative to a completely ice-free soil. Intermediate distributions of subsurface ice will modulate the mean annual surface temperatures between these extremes. If ice exists only deep within the regolith (*i.e.,* below several annual skin depths), its effect on the surface temperature will be small, as exhibited by the closeness ($\sim$1 K difference) of the pore-ice-free case (light solid black line) and the case with no accumulated pore ice, but $Z_{\rm mi} = 10$ m (heavy grey dashed line). Shallow pore ice more effectively changes the mean temperatures experienced at the surface. If $Z_{\rm mi} = 10$ m but pore ice deposits in the shallow depths below 8 cm, the mean annual surface temperature is $\sim$6 K higher than the case with no pore ice.

The Phoenix lander is incapable of excavating more than approximately 0.5 m into the regolith, and may be limited to even shallower depths if the ice table is shallow and has a high cohesive strength. Ground-penetrating radars on orbiting spacecraft do not currently have the resolution to discern ice distributions within the upper 10-15 m of the surface. Observations of mean annual temperatures and comparisons between these observations and models are the only presently available means to determine at what depth a shallow massive ice sheet may exist at high latitudes. The accuracy of subsurface and surface temperature models will be improved by Phoenix's measurements of regolith thermal properties with the Thermal and Electrical Conductivity Probe (TECP). Combined with Phoenix's measurements of ice table depth and (possibly) ice content in the shallow ice-bearing layers, mean annual surface temperature observations will constrain the depth range of a massive or pore-filling subsurface ice sheet. If ground-truth thermal properties from the Phoenix site are adjusted for locale-specific thermal inertias and albedos, then limits on massive ice sheet depths in other high-latitude regions may be assessed.

The Phoenix lander's robot arm will excavate into the surface regolith and deliver samples to the spacecraft deck for analysis. The stereoscopic imager, robotic arm camera, and the microscopy suite on MECA (Microscopy, Electrochemistry, and Conductivity Analyzer) cover a resolution range extending below 1 micron. Measurements of regolith particle sizes and shapes will help constrain the expected diffusion coefficient of the surface regolith. The cohesive strength of the regolith will also reveal, via observations of required digging power and the appearance of any coherent surface crusts, whether the effects of cementing agents such as salts may have acted to reduce the diffusivity,

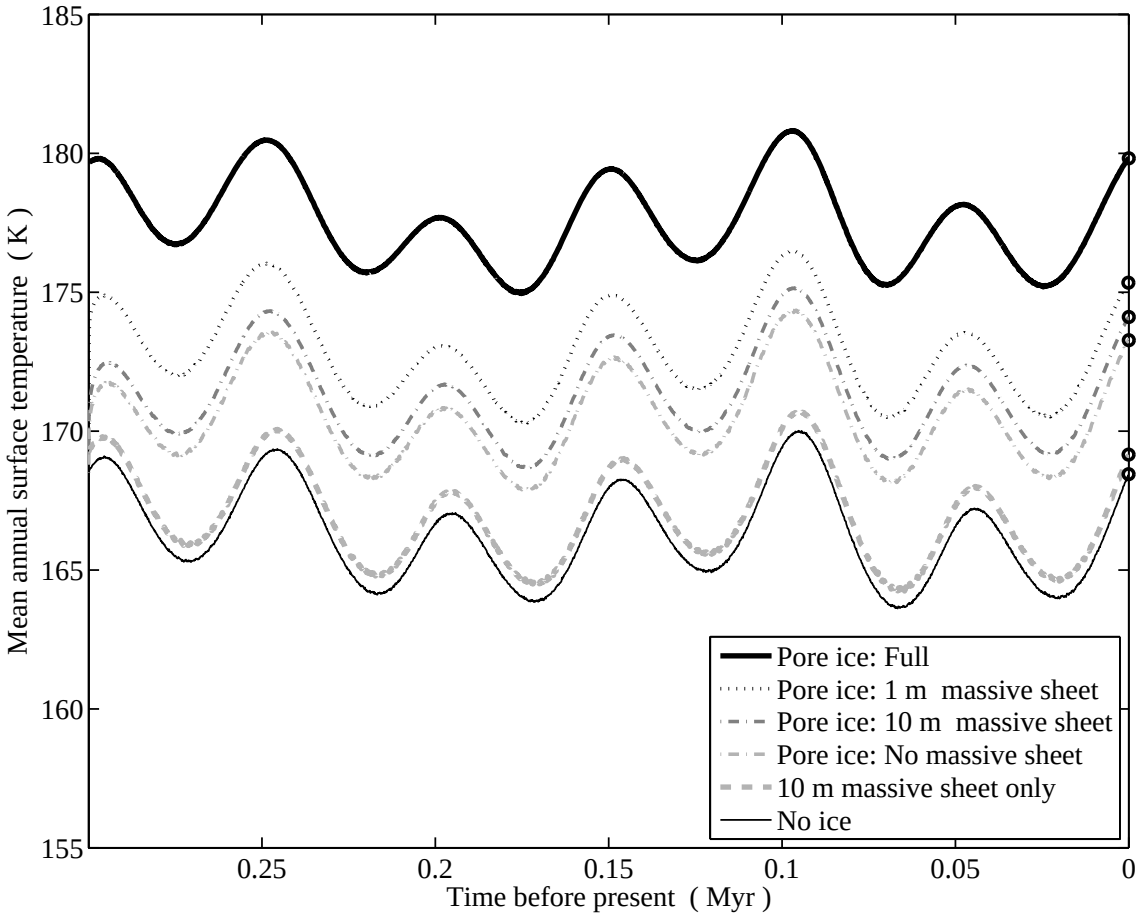

Figure 6.10: Mean annual surface temperatures differ depending on the subsurface ice content. The possible range is bracketed by an ice-free and ice-filled (excepting an 8-cm-thick ice-free surface layer) regolith. The difference between these extremes is 10 K, representing the range within which annual surface temperature deviations may fall. Also shown between these extremes are: two cases wherein pore ice deposits beneath a dry layer of 8 cm thickness (dash-dotted lines), one of which contains a massive sheet of pore-filling ice below 10 m (darker gray); and a third intermediate case with a massive ice sheet below 10 m, but no shallow pore ice (gray dashed line). The two cases which deposit pore ice exhibit an approximately 1 K difference in mean annual temperature. The case with a deep massive ice sheet but no pore ice is also about 1 K warmer than the case with no pore ice at all. These differences may permit the presence and depth of a massive ice sheet to be determined from seasonal temperature observations obtained from orbiting instruments.

as seen in Chapeter 4. At some shallow depth, Phoenix is expected to encounter ice-cemented soil. The depth of this ice table will represent ground-truth, to be compared to the various observations and models used to predict ice table depth. These measurements will be combined with estimates of the regolith diffusion coefficient to evaluate the proximity of the ice table to its equilibrium depth and the resulting implications for climate at the Phoenix site and throughout Mars' north polar region.

It is not known if the robot arm on Phoenix will be able to penetrate an ice-cemented soil, even

if the filling fraction is significantly less than 100%. The predictions of these and other models (*Schorghofer*, 2007; *Mellon et al.*, 2008) are that the region of the subsurface accessible to Phoenix will exhibit pore-filling, rather than pure ice. Given the instruments available, precise determinations of the filling fraction of these soils will be difficult. Raspings from the surface of the ice table, observed either through microscopy or a sublimating tailings pile, may constrain the relative fractions of ice and soil in the near-surface cryosphere. These model investigations suggest that at the depth of the ice table, the filling fraction will be between ∼70–90%. If a smaller filling fraction is observed, this would indicate an ice loss event more recent than 300 kya. The timing of such an event may be constrained by the observed ice contents and present ice table depth. Conversely, ice contents observed to be greater than ∼70–90% would be a strong indicator of a massive ice sheet within 0.5 m of the surface.

High latitude regions exhibit some shallow equilibrium ice table depth at all obliquities between 15 and 45 degrees (*Mellon and Jakosky*, 1993; *Feldman et al.*, 2005). Ice in these regions below a certain depth may survive periodic ice loss events. When the climate switches from a state that favors accumulation to one that favors loss, the ice table will retreat. Though ice at all depths may be unstable with respect to the atmosphere, its vapor pressure will still be set by the local temperature. If the assumption of saturated pore gas remains valid, ice beneath the ice table will continue to migrate downward even as the ice table descends. Low diffusivity of the overlying regolith, low subsurface temperatures in high-latitude regions, or high atmospheric vapor content may induce a relatively low rate of ice loss from the ice table. If the rate of ice table retreat is not sufficient to remove all subsurface ice by the time the climate again becomes favorable to ice preservation or growth, then deep subsurface ice may survive many cycles of climate change.

The deep ice carries information about past climate conditions through its abundance and depth distribution. The maximum depth of loss from a particular event may be recorded as an abrupt jump in the subsurface ice content, since the ice table interface will remain sharp as it retreats during a loss event. When accumulation is again favored, ice will grow throughout the region below the new equilibrium depth. Though the saturated vapor density of the pore space is independent of the filling fraction, the ice accumulation rate is modulated by the gradient in the diffusion coefficient, which will be steep across such an interface. Over time, the formerly sharp interface at the previous ice table depth will be softened as the relatively ice-poor regolith accumulates ice faster than the ice-rich region that has a more constricted diffusivity. Such local maxima in ice content profiles encode the history of local temperature and humidity environments and may be interpretable with models incorporating ice-loss events.

At depths between 10–15 m, the model indicates only minor accumulation of ice in 300 kyr if the initial state is ice-free. If protected from removal events by the overlying ice-rich pore spaces, the accumulation will continue unperturbed at these depths. Such deep ice may grow to fill a

substantial fraction of the pore space over long times. If these depths remain in diffusive contact with the atmosphere, isotopic climate tracers from epochs many obliquity cycles before the present may become trapped as the growing ice isolates pore spaces and produces bubbles.

The last decade has seen the theoretical and numerical prediction of ground ice on Mars, its detection from orbit, and immiment sampling expected from the Phoenix Lander. Equilibrium models have progressed dramatically; understanding the dynamics of subsurface ice position, loss, and exchange is ongoing. Experimental investigations and *in situ*observations continue to expand and enhance the understanding of these important processes in the Mars water cycle.